Optimization of L-shell X-ray fluorescence detection of lead in bone phantoms using synchrotron radiation

Mihai R. Gherase[1], Renfei Feng[2], David E. B. Fleming[3]

[1]California State University, Fresno, Fresno, California, 93740 United States
[2]Canadian Light Source, Saskatoon, Saskatchewan, S7N 2V3 Canada
[3]Mount Allison University, Sackville, New Brunswick, E4L 1E4 Canada

Abstract

Closely-related toxicity and retention mechanisms of lead (Pb) in the human body involve the bone tissues where Pb can accumulate and reside on a time scale ranging from years to tens of years. *In vivo* measurements of bone Pb can, therefore, play an important role in a comprehensive health risk assessment of Pb exposure. *In vivo* L-shell X-ray fluorescence (LXRF) measurement of bone Pb was first demonstrated over four decades ago. Implementation of the method, however, encountered challenges associated with low sensitivity and calibration procedure. In this study the LXRF measurement was optimized by varying the incident photon energy and the excitation-detection geometry. The Canadian Light Source synchrotron radiation was used to compare two different excitation-detection geometries of 90° and 135° using three different X-ray photon energies: 15.8, 16.6, and 17.5 keV. These energies optimized excitation of the L_3 subshell of Pb and simulated the most intense K-shell emissions of zirconium, niobium, and molybdenum, respectively. Five rectangular plaster-of-Paris bone phantoms with Pb concentrations of 0, 7, 17, 26, and 34 μg/g and one rectangular 3.1 mm-thick resin phantom mimicked the X-ray attenuation properties of human bone and soft tissue, respectively. Optimal LXRF detection was obtained by the 15.8 keV energy and the 90° and 135° geometries for the bare bone and the bone and soft tissue phantoms, respectively.

Introduction

The adverse health effects of lead are known since antiquity[1]. It is also known that bone tissues play an important role in the accumulation, metabolism, toxicity, and kinetics of lead in the human body[1]-[3]. It was estimated that the biological half-life of lead in bone ranges from several years to tens of years (ref. [4] and references therein). Therefore, bone lead measurements are considered valuable in the health risks assessment of long-term lead exposure. The first *in vivo* X-ray fluorescence (XRF) measurements of lead in the human bone were reported in 1976 by Ahlgren *et al.*[5]. They used the 122 keV γ-ray photons emitted by ^{57}Co to excite the K-shell of lead. Within the following decade two other XRF systems were developed: (i) tibia bone measurement using an L-shell XRF (LXRF) method by Wielopolski *et al.*[6] and (ii) K-shell XRF (KXRF) method using the 88 keV γ-ray photons emitted by ^{109}Cd by Laird *et al.*[7] and Somervaille *et al.*[8]. KXRF method using the ^{109}Cd was most widely adopted[4]. Although the initial LXRF method used the γ-ray photons from the ^{125}I radioisotope[6] for lead excitation, a later study utilized the partially plane polarized radiation of an X-ray tube[9]. The change is to be noticeable since the use of the X-ray tube radiation can avoid the many procedural difficulties and costs associated with the strictly-regulated production, storage, and transport of radioisotopes. Experimental and theoretical considerations of the X-ray tube LXRF method were later investigated by Todd[10] [11]. Using an X-ray tube with a molybdenum (Mo) target, Todd found that a secondary Mo target LXRF method optimized lead L-shell excitation and yielded higher signal-to-background ratios for the Pb L_α and Pb L_β peaks than those obtained using the plane polarized LXRF method that minimized the Compton scatter background[11]. In a separate study Todd *et al.*[12] compared the measurements of lead content of adult human cadaver tibiae as performed by the optimized LXRF method and electrothermal atomic absorption (AAS). Their results indicated "reasonably good" agreement for bare bone measurements, but poor results for intact leg measurements[12]. The poor accuracy and precision of the results were linked to the calibration methodology in which the X-ray attenuation of the soft tissue overlying the bone[10] had to be taken into account. The authors also highlighted the large variability of the LXRF data taken at various locations along the bare bone and the intact leg which were independent of the calibration method.

It is important to notice that in the first two decades researchers used or adapted existent X-ray tube and detector technology. The X-ray beam polarization, filtration, collimation, and

secondary target methods were the only techniques available that were employed in the several aforementioned studies. The absence of readily available intense and highly collimated X-ray beams precluded past LXRF researchers from systematic detailed investigations of the excitation-detection geometry. In the past two decades there were significant advances in the applications and manufacturing of polycapillary X-ray lenses[13] [14]. These passive devices can yield highly collimated intense hard X-ray beams using conventional X-ray tube technology[14] and allow more precise XRF geometries than the collimator-limited methods employed in the past. Simultaneously, progress in the miniature X-ray tube and electronically-cooled X-ray detector technologies led to the rapid increase in the commercial availability and performance of portable XRF spectrometers[15]. Relatively recent publications investigated the performance of these instruments for lead bone LXRF measurements[16]-[18]. Bare bone and bone with overlying materials of varying thickness phantoms were used in these studies to mimic the bone and soft tissue X-ray attenuation of *in vivo* LXRF experiments. The detection limits of lead varied roughly between 3 μg/g and 43 μg/g which matched or exceeded the performance of past LXRF dedicated spectrometers without any special modifications or additions to these general-purpose instruments. These advances in the XRF instrumentation indicate that further improvements of the lead LXRF method are possible. These concern both the *in vivo* lead detection limits and the important aspects regarding practical implementations. A review of the literature also seems to indicate that the fundamental limitations of bone lead LXRF detection are yet to be reached by experiments. In addition, since a cadaver bone lead study[12] showed high variability in results for both bare bone and intact measurements, the LXRF method was judged to be unreliable and a more rigorous soft tissue X-ray attenuation correction method[10] was not implemented. No alternative solutions were investigated until more recently[17].

Synchrotron radiation, one rectangular 3.1 mm-thick soft tissue phantom, and five bone phantoms which were doped with lead in five different concentrations (0, 7, 17, 27, and 34 μg/g) were used in this study to investigate the effects of the incident photon energy and the excitation-detection geometry on the bone lead LXRF detection for both the bare bone and the bone and soft tissue phantoms. Three properties of the synchrotron X-ray beam were essential to this approach: (i) monochromaticity, (ii) collimation, and (iii) high photon fluence rate. Two calibration lines corresponding to the amplitude measurements of the Pb L_α and Pb L_β peaks were obtained for each of the six combinations of photon-energy and excitation-detection

geometry experimental sets. The sensitivity of the LXRF measurements was evaluated using the slope values of the calibration lines. The Pb L_β/L_α ratio was calculated as the slope ratio of the Pb L_β and Pb L_α calibration lines. Soft tissue thickness was determined based on the relationship between atomic and measured Pb L_β/L_α ratios. An *ad-hoc* lead concentration measurement method based on the Pb L_β/L_α ratio measurements without the soft tissue attenuation correction was tested and its results were discussed.

Materials and Methods

The experiments were conducted at the Very Sensitive Elemental and Structural Probe Employing Radiation from a Synchrotron (VESPERS) beamline from the Canadian Light Source (CLS) synchrotron facility. A view from the top schematic of the XRF experimental setup for the 90° excitation-detection geometry is shown in Figure 1. In the 135° geometry the detector was rotated by 45° angle while preserving the same detector-sample distance. The detector was set in the polarization plane of the incident X-ray beam (horizontal plane). The entire experimental setup was placed in a lead hutch for radiation shielding. Due to the presence of lead walls a custom-made tapered copper cone with a 1.5 cm diameter aperture was placed between the detector and the sample as depicted in Figure 1. This procedure eliminated the stray lead X-rays originated in the walls or the adjacent equipment from reaching the detector. The X-ray photons emerging from the sample were detected by a four-element silicon drift detector (SDD) Vortex-ME4 (Hitachi High-Technologies Science America, Torrance, CA). In all XRF experiments the monochromatic X-ray beam with a 1.6% bandpass was used. The flux of X-ray beam was monitored continuously by two ion chambers filled with nitrogen (N_2) gas. The lead-doped bone phantoms were used in a previous LXRF study[16] and the fabrication procedure is described therein. Briefly, calcium sulphate hemihydrate ($CaSO_4 \cdot 1/2\,H_2O$), also known as plaster-of-Paris, was mixed with distilled water and then with a pipette-measured volume of lead atomic absorption spectrometry standard solution (Sigma-Aldrich, Oakville, ON). The mixture was then poured into a clear acrylic tube (Laid Plastics, Moncton, NB) with an inner square cross section of 2.2×2.2 cm^2. Solidification over a time period on the order of 2-3 weeks consisted in the evaporation of the residual water and subsequent formation of the solid plaster-of-Paris compound also known as calcium sulphate dihydrate ($CaSO_4 \cdot 2H_2O$). Following this procedure, the lead concentration was calculated based on the measured total mass of the solid bone

phantom and the known lead amount introduced for each sample. Five bone phantoms with lead mass concentrations of 0, 7, 17, 26, and 34 μg/g were used in this study. The soft tissue phantom was made using a commercially-available polyester resin kit (Bondo Corp., Atlanta, GA). The sample was made by pouring the liquid resin into a shallow circular plastic mold. Polymerization reaction solidified the circular phantom from which a square piece (2×2 cm^2) and 3.1 mm thickness was cut with a band saw to match the dimensions of the bone phantom. The resin was used as skin phantom in previous XRF studies[16] [19] and its combined elemental composition and density yield X-ray attenuation properties similar to those of soft tissues.

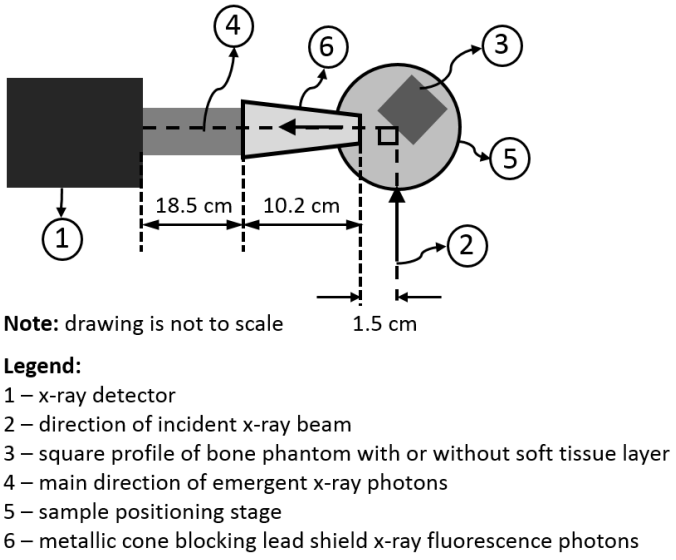

Figure 1. View from the top schematic of the XRF experimental setup from the VESPERS beamline at the CLS synchrotron research facility.

For experiments mimicking the bone and overlying soft tissue, the square soft tissue resin phantom was securely attached to one of the bone flat surfaces using a thin rubber band at one of the upper or lower edges of the soft tissue phantom. The soft tissue phantom surface was slightly abrasive which allowed small residual quantities of the bone phantom material to adhere on the

soft tissue phantom surface. This visually noticeable cross contamination was eliminated by cleaning thoroughly the soft tissue phantom surface with one or two alcohol-damped disposable cleaning tissues after each experiment.

Statistical data analysis and plotting was performed using the Origin 9.6 software (OriginLab, Corp., Northampton, MA). Microsoft Office Excel software (Microsoft Corp., Redmond, WA) was also used for simple repeated calculations and data organization and visualization. The lead XRF peaks Pb L_α and Pb L_β were fitted using a Gaussian function with a linear background:

$$y(x) = b + a \cdot x + A \cdot \exp[-(x - x_0)^2/2w^2]. \quad (1)$$

In equation (1) parameters a and b were the linear background fit parameters while A, x_0, and w were the amplitude (or peak height), center, and width Gaussian peak parameters, respectively. The peak amplitude A was selected as the XRF line intensity metric. Variables x and y represented X-ray photon energy and XRF intensity (i.e., number of counts), respectively. To compare each peak width with the expected energy resolution values of the detector, the Full Width at Half Maximum ($FWHM$) was also calculated based on the width parameter w value:

$$FWHM = w \cdot \sqrt{2 \ln 2}. \quad (2)$$

The reduced chi-squared value (χ^2/n) and the visual representation of fitted function $y(x)$ were monitored and used as goodness-of-fit metrics during the peak data analysis.

The variations of the synchrotron X-ray beam output were corrected following the peak fitting procedure. The correction procedure used the sum of the counts N_{sum} recorded in all channels after each XRF experiment as follows. The corrected peak amplitude $A_{cor,i}$ corresponding to measurement i was given by:

$$A_{corr,i} = A_i \cdot \frac{N_{sum,i}}{N_{sum,0}}. \quad (3)$$

In equation (3) the notations $N_{sum,i}$ and $N_{sum,0}$ refer to sum of recorded counts corresponding to measurement i and 0, respectively. The measurement index i ranged from 0 to 4 corresponding to increasing bone lead concentrations from 0 $\mu g/g$ to 34 $\mu g/g$.

Results and Discussion

Calibration lines results and analysis

To simplify referencing to the all the experiments in this study, labels were created and subsequently used. The abbreviation procedure is explained in Table 1.

	Bare bone phantoms			Bone & soft tissue phantom		
Excitation-detection angle	Incident photon energy (keV)			Incident photon energy (keV)		
	15.8	16.6	17.5	15.8	16.6	17.5
90°	bb-90-15.8	bb-90-16.6	bb-90-17.5	st-90-15.8	st-90-16.6	st-90-17.5
135°	bb-135-15.8	bb-135-16.6	bb-135-17.5	st-135-15.8	st-135-16.6	st-135-17.5

Table 1. Abbreviations used for experiment labels. The label elements separated by the dash line identify, from left to right, the phantom type, the excitation-detection angle, and the excitation or incident X-ray photon energy.

Two samples of the acquired XRF spectra for the bare bone and the bone with overlying soft tissue are shown in Figure 2.

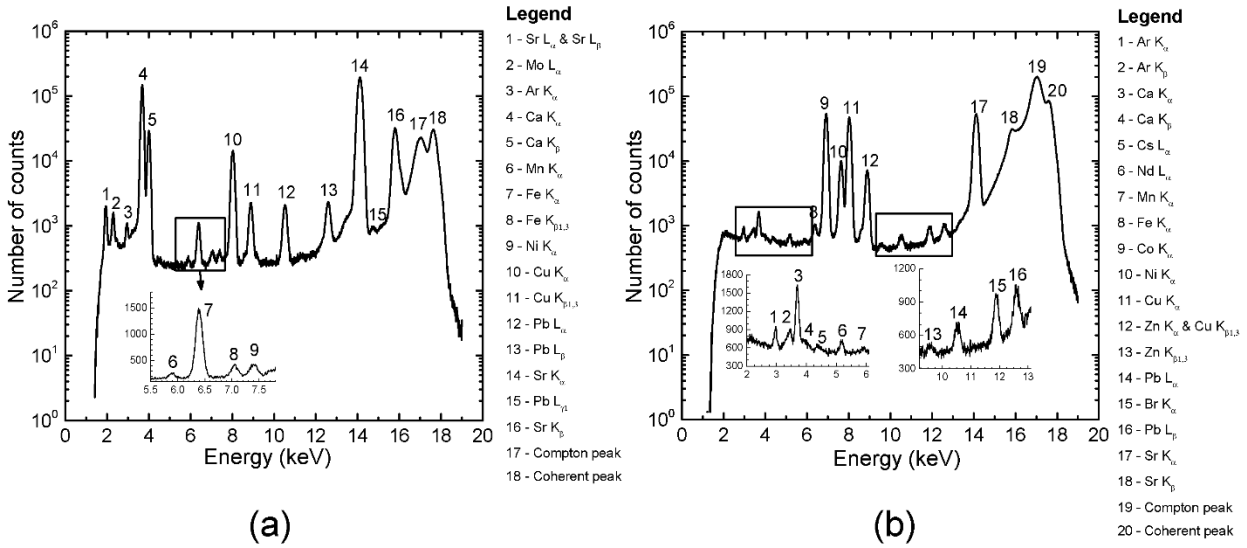

Figure 2. Semi-logarithmic plots of two XRF spectra acquired in experiments bb-90-17.5 (a) and st-90-17.5 (b) at the maximum bone phantom lead concentration of 75 μg/g.

The XRF peaks in the spectra from Figure 2 identify elements originating from the bone and soft tissue samples as well as metallic equipment parts in the immediate proximity of the X-ray detector. In the XRF spectrum from plot (b) significantly decreased amplitude of the XRF peaks of calcium (Ca), strontium (Sr), and lead (Pb) as compared to those from the XRF spectrum in plot (a) can be noticed. This is the effect of the soft tissue X-ray attenuation. A significantly larger backscatter peak (Compton and coherent) is also evident in the X-ray spectrum (b) due to the increased X-ray scattered events within the bone and soft tissue phantom that reach the detector. Samples of the Pb L_α and Pb L_β fitted peaks are shown in Figure 3 for the minimum and maximum lead concentrations of 0 and 75 μg/g. The two panels (a) and (b) in the figure correspond to bb-135-17.5 and st-135-17.5 experiments. The Br K_α peak was previously noticed and thought to originate in the bromine from the resin soft tissue phantoms[16]. However, a slightly decreased amplitude Br K_α peak was observed in the bare bone phantoms as well, hence, the bromine in the resin material might not have been the solely contaminant.

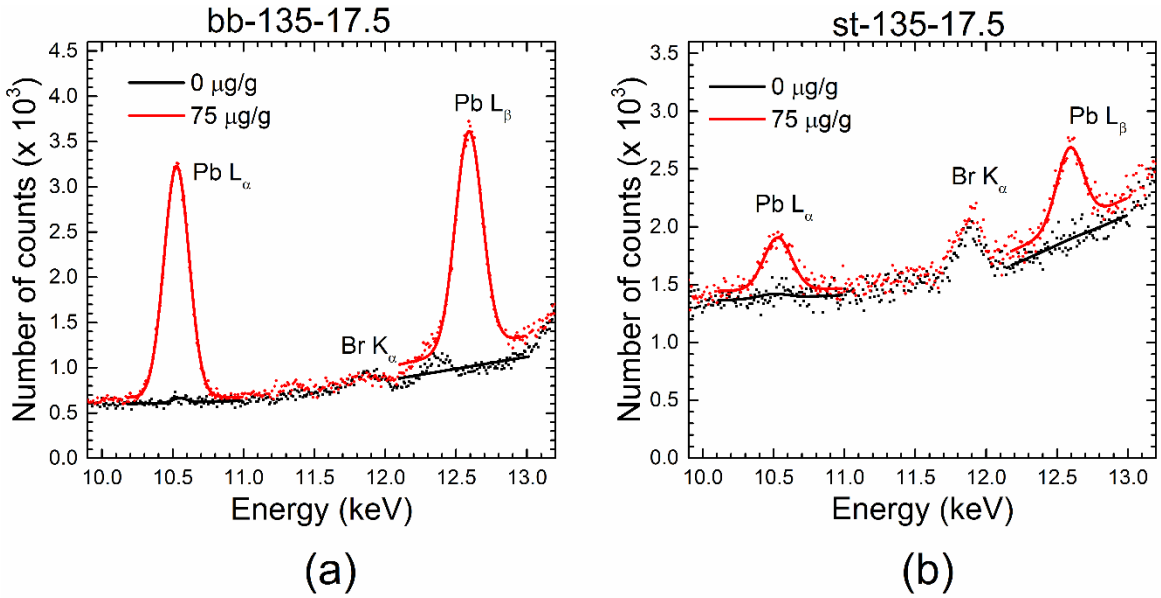

Figure 3. Sample plots of the fitted Pb L_α and Pb L_β peaks and corresponding acquired data for two lead concentrations: 0 μg/g (black lines and dots) and 75 μg/g (red lines and dots). As indicated the two panels correspond to experiments bb-135-17.5 (a) and st-135-17.5 (b).

A sample of the calibration lines obtained for the 90° excitation-detection angle are shown in the panel plots of Figure 4. The left-hand panels (a) and (c) and the right-hand panels (b) and (d) used the Pb L_α and Pb L_β data, respectively. The upper panels (a) and (b) and the lower panels (c) and (d) correspond to the bare bone phantom and bone and soft tissue phantoms experiments, respectively. In the plots of the upper panels (a) and (b) it can be noticed that the slope values of

the bare bone phantom calibration lines are inversely proportional with incident photon energy. This is expected since maximum XRF excitation is achieved by minimum energy gap between the incident photon energy and L_2 and L_3 subshell edges at 15.2 keV and 13.0 keV[20]. The direct interpretation of the bone and soft tissue calibration lines shown in panels (c) and (d) is more difficult due to the increased backscatter and X-ray attenuation of the soft tissue.

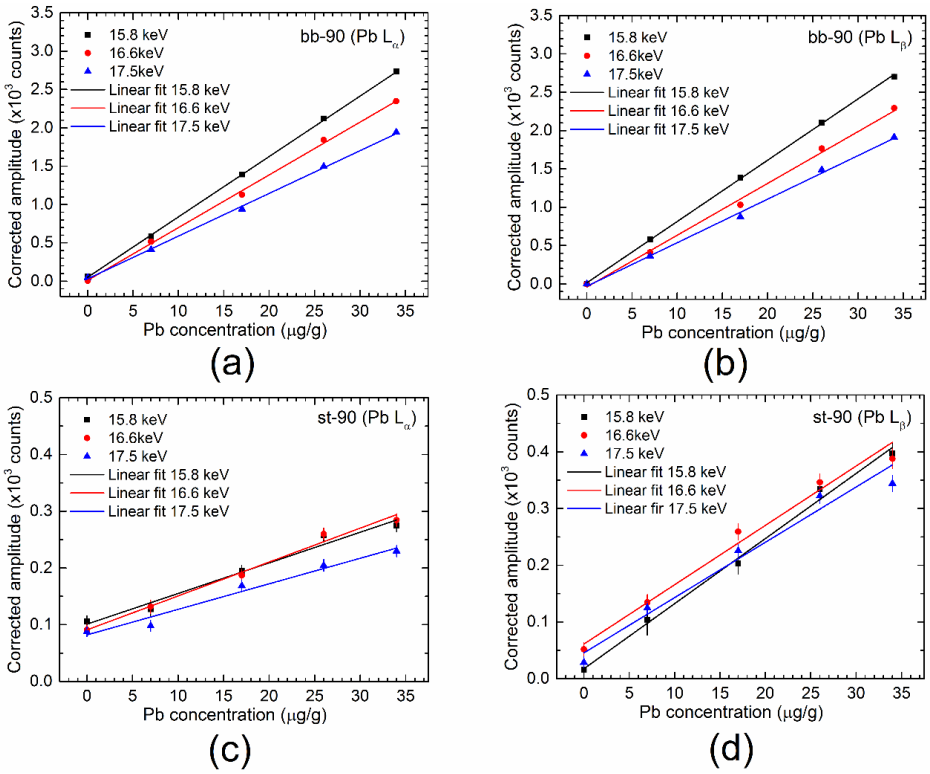

Figure 4. Four panel plots of the calibration lines and data corresponding to the 90° excitation-detection geometry. In upper panels (a) and (b) corresponding to the bare bone phantoms the data error bars are not visible due to their small size.

The slope values dependence on the incident photon energy can be more easily analyzed and interpreted in the data provided in Table 2 and in the plots from Figure 5. The two panel plots (a) and (b) of Figure 5 show the slope values for the Pb Lα and Pb Lβ peaks. It can be seen that the incident energy dependence of the slope values observed for the bare bone phantoms is significantly reduced for the slope values corresponding to the bone and soft tissue phantoms due to increased attenuation. Visual inspection of the plots also reveals that the 135° excitation-detection geometry provided better sensitivity for lead detection at all three incident photon energies for both the bare bone (bb) and the bone and soft tissue samples (st). This can be explained by the reduced soft tissue x-ray attenuation given by the shorter photon pathlength of

Pb L_α and Pb L_β in this geometry. Further analysis of this evidence based on the lead L_β/L_α ratio is provided later in this section. Also, the slope values corresponding to the Pb L_β data are slightly higher than those of Pb L_α in the case of the bone and soft tissue phantom experiments. This can be accounted for by the higher photon energy (12.6 keV) of the Pb L_β comparing to that of Pb L_α (10.5 keV) which diminished the effect of the soft tissue X-ray attenuation. Positive *y*-intercept values (at the 95% confidence level) were also noticed for five out of the nine results corresponding to the Pb L_α peak data (third column of Table 2).

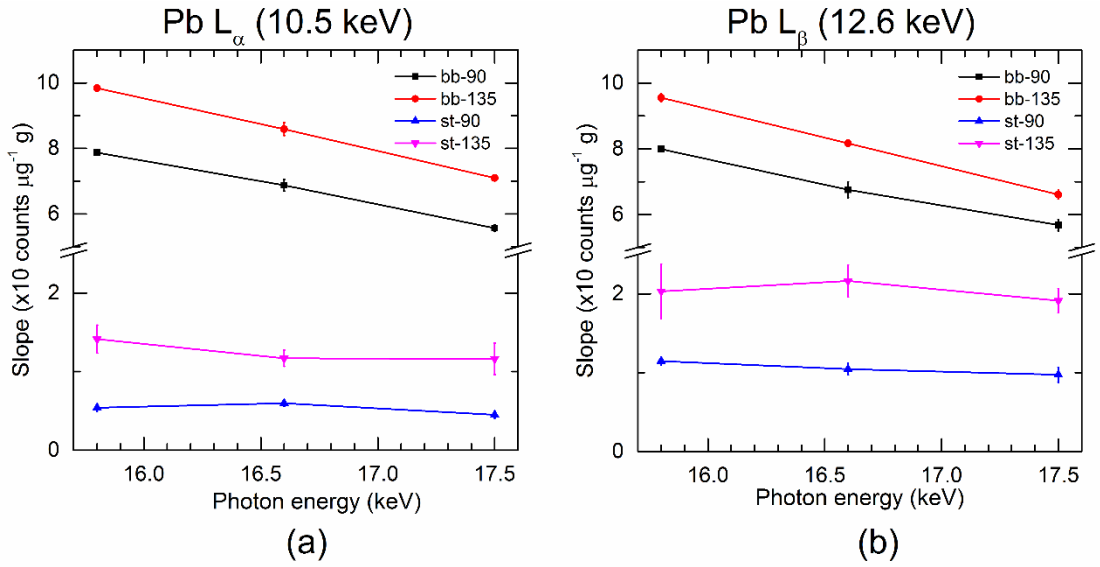

Figure 5. The plot of the slope values as a function of the incident photon energy. The straight lines connecting the data points corresponding to a particular pair of the bone phantom and excitation-detection geometry were added to ease the visualization of the trends.

Experiment	Pb L_α			Pb L_β		
	Slope (counts $\cdot$ µg^{-1} $\cdot$ g)	*y*-intercept (× 10 counts)	χ^2/n	Slope (counts $\cdot$ µg^{-1} $\cdot$ g)	*y*-intercept (× 10 counts)	χ^2/n
bb-90-15.8	78.2(8)	5.2(8)	2.9	79.9(7)	2(1)	1.8
bb-90-16.6	69(2)	1(3)	10.3	68(2)	-4(4)	6.1
bb-90-17.5	56(1)	3(2)	4.6	57(2)	-3(3)	4.4
bb-135-15.8	98.4(7)	4.9(9)	1.2	96(1)	-2(2)	2.5
bb-135-16.6	86(2)	3(3)	10.2	81.7(9)	-2(2)	1.2
bb-135-17.5	71.0(8)	2(1)	2.1	66(1)	-2(3)	2.4
st-90-15.8	5.4(5)	10.1(9)	1.2	11.5(5)	2(1)	0.5
st-90-16.6	6.0(4)	9.1(8)	0.9	10.5(8)	6(1)	2.0
st-90-17.5	4.5(4)	8.2(9)	1.5	9.7(9)	5(2)	4.3
st-135-15.8	14(2)	6(3)	2.9	20(3)	-3(7)	4.6
st-135-16.6	12(1)	6(3)	0.6	20(2)	-1(4)	2.4

st-135-17.5	12(2)	5(5)	5.0	19(1)	-1(3)	2.4

Table 2. Slope and y-intercept values obtained from the linear fitting procedure yielding the calibration lines. The one significant figure uncertainties corresponding to the last significant figure of the parameter value are given in the round parentheses.

It is well-known that As K_α energy overlaps with that of Pb L_α at roughly 10.5 keV and the two energies cannot be distinguished within the energy resolution limits of current X-ray detectors[10]. Hence, trace amounts of arsenic in the soft tissue and/or bone phantom materials may account for the observation. A more plausible explanation of this results is the inherent randomness of the calibration lines data as indicated by the large range (0.5 – 10.3) of the reduced chi-squared values provided in Table 2. In 8 cases out of the total of 24, the reduced chi-squared values were larger than 3. According to the chi-squared probability distribution corresponding to three degrees-of-freedom ($n = 5 - 2 = 3$), the probability of such occurrences is only 2.9% [21]. The result was not a consequence of large deviations from linearity in the data. For example, see the linear fit indicated by the red color in plot (a) from Figure 4; the high linearity of the data which can observed graphically corresponds to a large chi-squared value of 10.3 (see 2-nd row and 4-th column in Table 2). The result is rather the effect of underestimating the uncertainties associated with the fitted amplitude of the Pb L_α and Pb L_β peaks. The counting statistics errors resulting from the peak fitting procedure did not take into account systematic uncertainties that proved to be significant. The most important were considered to be small three-dimensional inhomogeneity regions existent in both the bone and the soft tissue phantom materials. The inhomogeneity consisted of small air bubbles which are unavoidably trapped within both the plaster-of-Paris and the resin during the solidification process. This not only had the effect of local variations of the lead concentration in the bone phantoms, but also led to variations in the linear X-ray attenuation coefficient along different photon pathways. Although consistency amongst all measurements was planned during the experimental procedures of the data acquisition, it was virtually impossible to arrange such that the X-ray beam would be incident on the same bare bone phantom or bare bone phantom and soft tissue phantom combination in precisely the same point. Hence, systematic uncertainties were introduced and are reflected in the large observed range of chi-squared values. The inhomogeneity effect on the XRF data is particularly enhanced by the small size of the incident synchrotron X-ray beam and

was also noticed in the calibration data from a different synchrotron study which used arsenic-doped resin samples[22].

An insight regarding optimization of the bone lead detection can also be gained by the analysis of the background obtained during the peak fitting procedure. In general, a lower background is associated with a lower detection limit. The background value measured in number of counts at the peak energy was readily calculated using the fitting background parameters a and b identified in equation (1). The results are shown in the plot from Figure 6. For an easier identification of the trends, the corresponding uncertainties were not added. A decreasing trend with increasing incident photon energy is noticed for all experimental sets with the exception of the bare bone phantoms in the 90° excitation-detection geometry (bb-90). The observation is consistent with decreasing spectral overlap of the Pb L_α and Pb L_β peaks with the Compton and coherent scattering peaks with increasing incident photon energy. The trend is more pronounced for the bone and soft tissue phantoms due to an increase in the number of backscattered photons. The effect was also noticed in the semi-logarithmic plots shown in Figure 1. Due to the lower mass density and effective atomic number Z_{eff} of the soft tissue phantom a larger number of backscattered photons are able to "escape" the sample self-attenuation and reach the detector. The relative background plots from Figure 6 indicate a slightly higher 90° backscatter compared to the 135° one with the exception of three data points at the 15.8 and 17.5 keV photon energies where the relationship is inverted. Two factors may account for this observation. First, the range of photon scattering angles contributing to the background under the observed Pb L_α and Pb L_β peaks, although centered on the values of 90° and 135°, is mostly determined by the spatial extent of the detector. Therefore, the differences in the Compton scatter probabilities are reduced. Second, the intrinsic energy blurring of the X-ray detector further hinder differences in the observed spectra.

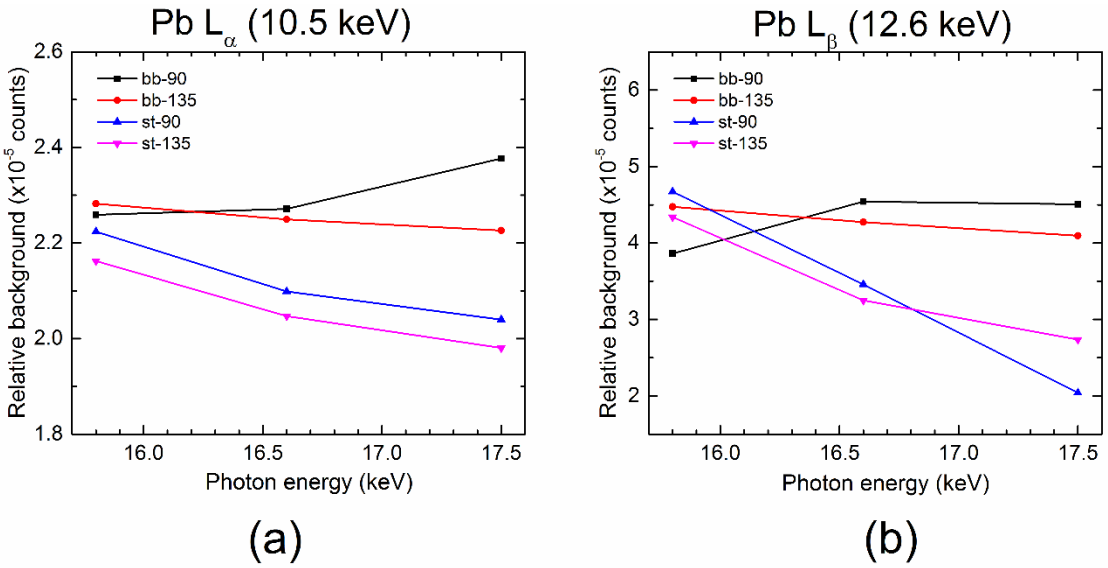

Figure 6. Relative background calculated as the ratio of the fitted background at each of the Pb L_α and Pb L_β peak energies and the sum of the total number of counts for each set of experiments.

Analysis of the measured Pb L_β/L_α ratio

Useful insights were also gained when the X-ray attenuation effect of the bone and soft tissue phantoms on the Pb L_β/L_α ratio was analyzed in detail. The unattenuated Pb L_β/L_α ratio was measured experimentally to be 1.043 ± 0.099 and the theoretical value was calculated to be 0.8943 at an incident photon energy of 17.8 keV[23]. If the theoretical value is used as reference, the attenuated Pb L_β/L_α ratio by a homogeneous layer of thickness t can be calculated using the following equation:

$$\text{Pb } L_\beta/L_\alpha = 0.8943\frac{\exp(-\mu_\beta t)}{\exp(-\mu_\alpha t)} = 0.8943\cdot\exp\left[\left(\mu_\alpha-\mu_\beta\right)\cdot t\right]. \quad (4)$$

In equation (4) symbols μ_α and μ_β denote the linear attenuation coefficients of the material at the energies of 10.5 and 12.6 keV corresponding to the average energies of the Pb L_α and Pb L_β X-ray emission lines. The exponent in equation (4) is a number larger than one since for any material $\mu_\alpha > \mu_\beta$. The linear attenuation coefficients can be calculated as the product between the mass attenuation coefficient and the material mass density. The mass attenuation coefficients of the plaster-of-Paris and resin materials were calculated based on their respective bulk elemental composition or chemical formula using the online XCOM database calculator[24]. The bulk elemental composition of resin was taken from the paper of Gawdzik *et al.*[25]. Table 3 shows the calculations of the linear attenuation coefficients for the resin and plaster-of-Paris materials at the two photon energies.

Material	Plaster-of-Paris		Resin	
Chemical formula/	$CaSO_4 \cdot 2H_2O$		[H] = 0.05	
Elemental composition			[C] = 0.60	
			[O] = 0.35	
Measured mass density (g/cm^3)	1.02		1.20	
Photon energy (keV)	10.5	12.6	10.5	12.6
Mass attenuation coefficient (cm^2/g)	29.51	17.49	3.060	1.825
Linear attenuation coefficient (cm^{-1})	30.10	17.84	3.672	2.190

Table 3. Calculations of the linear attenuation coefficients for the bone and soft tissue phantom materials at the 10.5 and 12.6 keV X-ray photon energies.

The attenuated Pb L_β/L_α was calculated as the ratio of the calibration line slopes corresponding to the lead L-shell peaks. The ratio values and their corresponding uncertainties were plotted for each incident photon energy in panels (a) and (b) in Figure 7. The exponential curve in plot (c) is the graphical representation of equation (4) using the corresponding bone phantom (plaster-of-Paris) linear attenuation coefficients from Table 3. The same equation was used to graph the two exponential curves (red and blue) in plot (d), however, the reference value of 0.894 was replaced by the corresponding bare bone Pb L_β/L_α ratio indicated in plot (a).

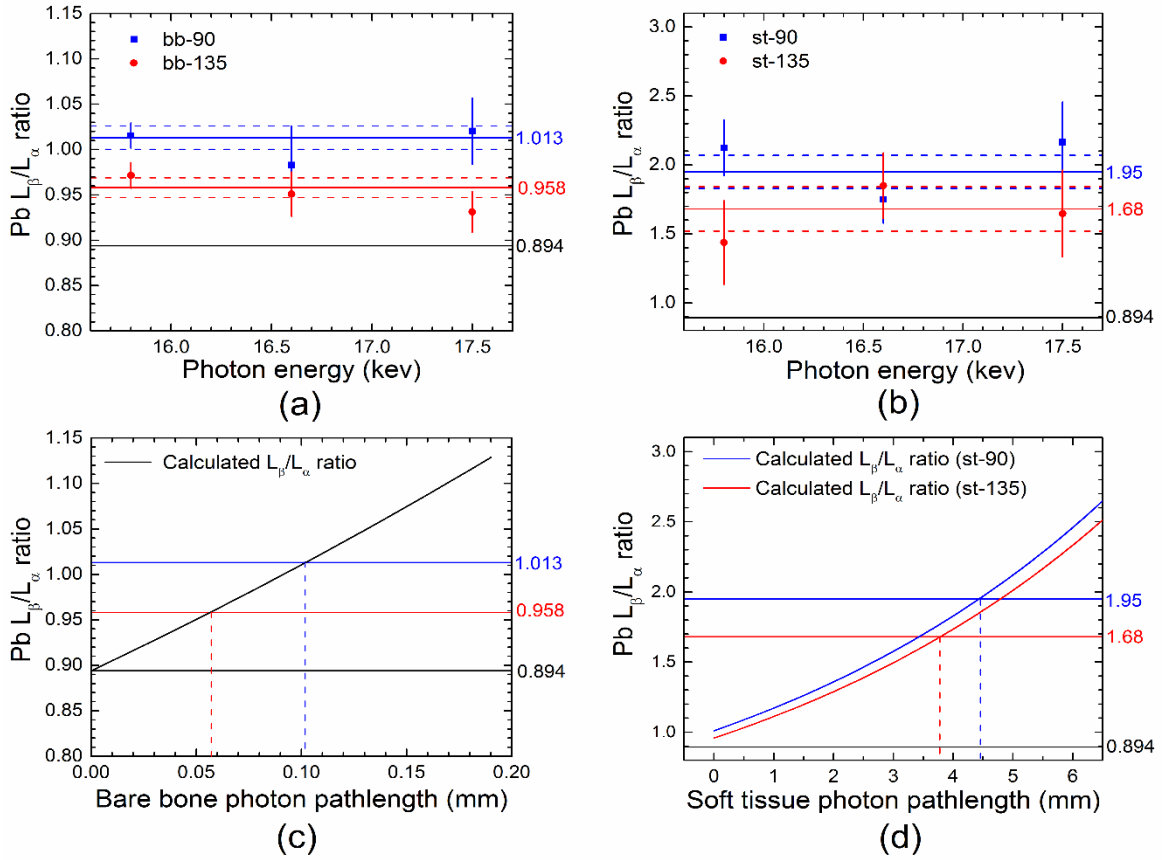

Figure 7. Plots of the Pb L_β/L_α ratio for the bare bone phantom experiments (a) and bone and soft tissue phantom experiments (b). The horizontal dashed lines indicate the boundaries of the one standard deviation interval as determined by the inverse-variance-weighted averaging of the three measurements. The average photon pathlength was estimated using Pb L_β/L_α ratio measurements and calculated Pb L_β/L_α ratio as a function of photon pathlength for the bone phantom (plaster-of-Paris) (c) and soft tissue (resin) (d). The blue and red colors identify the two excitation-detection geometries.

The photon pathlength in the bone phantom material was thus calculated to be on the order of 0.1 mm and 0.05 mm by using the average Pb L_β/L_α ratio from the 90° and 135° geometries, respectively. From plot (d) of Figure 7 the photon pathlength values in the soft tissue phantom material corresponding to the two geometries were determined to be around 4 mm. These values are consistent with the 3.1 mm thickness of the soft tissue phantom as shown in Figure 8. The photon pathlength value is minimal for the 135° geometry as can be deduced from a basic analysis of the two geometries depicted in Figure 8. The difference between the two values for the soft tissue indicated in plot (d) of Figure 7 is not statistically significant due to the large uncertainties of the measured Pb L_β/L_α values indicated by the dashed lines in the plot (b) of Figure 7. However, the slope values shown in the plots (a) and (b) of Figure 5 indicate

significantly higher values for the 135° geometry which is in agreement with the minimal X-ray attenuation of the Pb L_α and Pb L_β in this experimental setup.

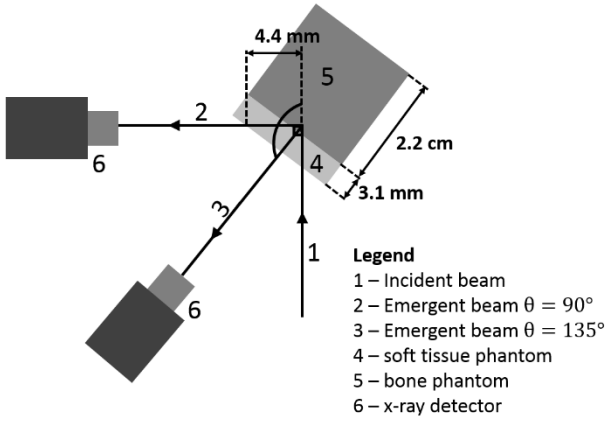

Figure 8. Schematic of the two excitation-detection geometries. Minimal photon pathlength in the soft tissue occurred for the scattering angle $\theta = 135°$.

Lead concentration calculations

In the above paragraph the analysis of the Pb L_β/L_α ratio led to an estimate of the average photon pathlength in the soft tissue layer. The analysis can be further extended to calculate Pb concentrations based only on the bare bone calibration lines and the bone and soft tissue phantom LXRF measurements. Using the same notations equation (4) can be re-written for the bone and soft tissue phantom LXRF measurements:

$$\left(\text{Pb } L_\beta/L_\alpha\right)_{st} = \left(\text{Pb } L_\beta/L_\alpha\right)_{bb} \times \exp\left[\left(\mu_\alpha - \mu_\beta\right)t\right]. \quad (5)$$

In equation (5) the sub-indices "st" and "bb" refer to the bone and soft tissue phantom and the bare bone LXRF measurements, respectively. The following notation is made to simplify the algebraic equations:

$$r = \left(\text{Pb } L_\beta/L_\alpha\right)_{st} / \left(\text{Pb } L_\beta/L_\alpha\right)_{bb}. \quad (6)$$

Hence,

$$t = \ln(r)/\left(\mu_\alpha - \mu_\beta\right). \quad (7)$$

The approximate relationships between the bone and soft tissue Pb L_α and Pb L_β peak amplitude denoted by $(\text{Pb } L_\alpha)_{st}$ and $\left(\text{Pb } L_\beta\right)_{st}$ and their bare bone equivalents $(\text{Pb } L_\alpha)_{bb,eq}$ and $(\text{Pb } L_\alpha)_{bb,eq}$ are based on the soft tissue attenuation of the incident photons corresponding to a pathlength of $\sqrt{2}t$ and of the Pb L_α and Pb L_β photons corresponding to a pathlength of t for the

135° excitation-detection geometry. Therefore, the lead concentration values for each lead LXRF peak are:

$$c_\alpha = (\text{Pb L}_\alpha)_{bb,eq}/\text{slope}_{bb,\alpha} = (\text{Pb L}_\alpha)_{st}/\text{slope}_{bb,\alpha} \times \exp\left[\left(\mu_\alpha + \mu_i\sqrt{2}\right)t\right], \quad (8)$$

$$c_\beta = \left(\text{Pb L}_\beta\right)_{bb,eq}/\text{slope}_{bb,\beta} = \left(\text{Pb L}_\beta\right)_{st}/\text{slope}_{bb,\beta} \times \exp\left[\left(\mu_\beta + \mu_i\sqrt{2}\right)t\right]. \quad (9)$$

Using equation (7) the results simplify to:

$$c_\alpha = (\text{Pb L}_\alpha)_{st}/\text{slope}_{bb,\alpha} \times r^{(\mu_\alpha+\mu_i\sqrt{2})/(\mu_\alpha-\mu_\beta)}, \quad (10)$$

$$c_\beta = \left(\text{Pb L}_\beta\right)_{st}/\text{slope}_{bb,\beta} \times r^{(\mu_\beta+\mu_i\sqrt{2})/(\mu_\alpha-\mu_\beta)}. \quad (11)$$

Table 4 shows a sample of such Pb concentration calculations using equations (11) and (11), the st-135-17.5 experimental data and the calibration lines obtained in the corresponding bb-135-17.5 experiments. The value of r was calculated using the slope values ratios from the two data sets.

$(\text{Pb L}_\alpha)_{st}$ counts	$(\text{Pb L}_\beta)_{st}$ counts	r	$\text{slope}_{bb,\alpha}$ g/μg	$\text{slope}_{bb,\beta}$ g/μg	$\frac{\mu_\alpha + \mu_i\sqrt{2}}{\mu_\alpha - \mu_\beta}$	$\frac{\mu_\beta + \mu_i\sqrt{2}}{\mu_\alpha - \mu_\beta}$	c_α μg/g	c_β μg/g	[Pb] μg/g
124	113	1.703	71	66	3.378	2.378	11	6	7
194	269						17	14	17
414	539						35	29	26
425	622						36	33	34

Table 4. Calculations of the lead concentrations from the bone and soft tissue data with 135° geometry and 17.5 keV incident photon energy.

The results shown in Table 4 are encouraging. However, two issues can be noted in relation to a possible translation to an *in vivo* technique: (i) *a priori* knowledge regarding soft tissue attenuation was used, and (ii) the value of r included the measured bone and soft tissue phantom Pb L_α and Pb L_β slope values. The method was developed *ad-hoc* in this section prompted by the results shown in Figure 7. Additional work has to be done towards its validation and is beyond the intended scope of this study. The effects of local variations in the X-ray attenuation coefficients, lead concentration, and uncertainties linked to the spectral measurements have to be thoroughly investigated in future studies. Todd[10] discussed at length the effects of the varying elemental composition and density of the soft tissues and bone as well as *in vivo* trace

concentrations of lead or arsenic: As K_α and Pb L_α peaks cannot be resolved at 10.5 keV using common X-ray detector energy resolution capabilities.

Implications for *in vivo* LXRF applications

Finally, the implications of these synchrotron-based experimental results to the more practical and affordable X-ray tube technology in foreseeable *in vivo* bone lead LXRF applications is discussed. Based on the results shown in Figure 5 no incident photon energy is indicated to produce significantly better LXRF lead detection for the bone with overlying soft tissue phantoms. For the bare bone phantoms the lowest 15.8 keV incident energy was optimal which points to a zirconium (Zr) filter for *in vivo* applications targeting bone sites with a thin soft tissue layer. When the X-ray tube target materials are solely considered, the 17.5 keV energy of molybdenum (Mo) is perhaps the better, more practical and feasible choice. This conclusion is based on the fact that Mo is known as a common X-ray tube target material[26]. The Mo X-ray tube technology is an integral part of the film-based mammography – a clinical X-ray imaging modality used for both the diagnosis and the screening of breast cancer [27]. The emitted K-line photon energies of Mo optimize the film-based image contrast between normal and cancerous tissues – a direct consequence of the measured X-ray attenuation differences between these breast tissues at various X-ray photon energies [28]. Technological and practical issues also concern incident beam collimation achieved by polycapillary X-ray lenses, high count rate X-ray detector capability, size, and cost. The capabilities of the synchrotron experimental setup used in this study are not likely to be readily reproduced by existent portable X-ray tube and detector technology. However, longer or repeated X-ray spectra acquisition procedures are only restricted by radiation dose considerations and may approach similar lead LXRF detection for a lower incident X-ray beam flux and smaller X-ray detector size.

Conclusions

Using a synchrotron X-ray beam and simple rectangular bone and soft tissue phantoms, it was found that the 135° excitation-detection geometry produced superior lead LXRF detection to that of the 90° geometry. This result was shown to be related to a reduced pathlength of the emitted

Pb L_α and Pb L_β X-ray photons which minimized the negative effects of the soft tissue X-ray attenuation. Future work using a different experimental setup may extend the geometry to larger angles approaching the 180° angle which would minimize the soft tissue attenuation of both the incident and the emitted X-ray photons. It is worth noting, however, that the larger angle geometries are only possible using small-size detectors which may reduce LXRF sensitivity. A possible solution is to group multiple individual low-cost small X-ray detectors around the direction of the incident beam. No incident photon energy amongst the three values of 15.8, 16.6, and 17.5 keV was found to produce a significantly better lead LXRF detection for the bone and soft tissue phantom arrangement. The positive effect of increased excitation by an incident photon energy closer to the L subshell edge value was counterbalanced by the negative effect of increased backscatter background in the observed X-ray spectra. The 17.5 keV photons produced by a Mo target X-ray tube was suggested as the better and, perhaps, more feasible approach.

Acknowledgements

M.G. would like to acknowledge the early stage contributions to the x-ray spectra data analysis of the undergraduate students Andressa Freire-Gama and Andres Vargas from the Department of Physics at the California State University, Fresno. M. G. would also like to acknowledge the travel financial support from the College of Science and Mathematics at the California State University, Fresno. D. F. would like to acknowledge the financial support of the Natural Sciences and Engineering Research Council (NSERC) of Canada Discovery grant #261523. Synchrotron measurements were performed at the Canadian Light Source, which is supported by the Canada Foundation for Innovation, Natural Sciences and Engineering Research Council of Canada, the University of Saskatchewan, the Government of Saskatchewan, Western Economic Diversification Canada, the National Research Council Canada, and the Canadian Institutes of Health Research.

References

[1] P. S. I. Barry, D. B. Mossman, *Brit. J. Industr. Med.* **1970**; *27*, 339.
[2] M. B. Rabinowitz, G. Wetherill, J. Kopple, *Science* **1973**; *182*, 725.
[3] M. B. Rabinowitz, *Environ. Health Perspective* **1991**; *91*, 33.
[4] D. R. Chettle, *X-ray Spectrom.* **2005**; *34*, 446.
[5] L. Ahlgren, K. Lidén, S. Mattson, S. Tejning, *Scand. J. Work Environ. Health* **1976**; *2*, 82.
[6] L. Wielopolski, J. F. Rosen, D. N. Slatkin, D. Vartsky, K. J. Ellis, S. H. Cohn, *Med. Phys.* **1983**; *10*, 248.
[7] E. E. Laird, D. R. Chettle, M. C. Scott, *Nucl. Instrum. Methods* **1982**; *193*, 377.

[8] L. J. Somervaille, D. R. Chettle, M. C. Scott, *Phys. Med. Biol.* **1985**; *30*, 929.
[9] L. Wielopolski, J. F. Rosen, D. N. Slatkin, R. Zhang, J. A. Kaelf-Ezra, J. C. Rothman, M. Maryanski, Jenks S. T., *Med. Phys.* **1989**; *16*, 521.
[10] A. C. Todd, *Phys. Med. Biol.* **2002**; *47*, 491.
[11] A. C Todd, *Phys. Med. Biol.* **2002**; *47*, 507.
[12] A. C. Todd, S. Carroll, C. Geraghty, F. A. Khan, E. l. Moshier, S. Tang, P. J. Parsons, *Phys. Med. Biol.* **2002**; *47*, 1399.
[13] C. A. MacDonald, W. M. Gibson, *X-ray Spectrom.* **2003**; *32*, 258.
[14] N. Gao, I. Y. Ponomarenko, *X-ray Spectrom.* **2003**; *32*, 186.
[15] S. Piorek, *Field Anal. Chem Technol.* **1997**; *1*, 317.
[16] D. E. B. Fleming, M. R. Gherase, K. M. Alexander, *X-ray Spectrom.* **2011**; *40*, 343.
[17] L. H. Nie, S. Sanchez, K. Newton, L. Grodzins, R. O. Cleveland, M. G. Weisskopf, *Phys. Med. Biol.* **2011**; *56*, N39.
[18] A. J. Specht, M. Weisskopf, L. H. Nie, *J. Biomarkers* **2014**; article ID 398032.
[19] R. C. N. Studinski, F. E. McNeill, D. R. Chettle, J. M. O'Meara, *X-ray Spectrom*. **2004**; *33*, 285.
[20] R. D. Deslattes, E. G. Kessler Jr., P. Indelicato, L. de Billy, E. Lindroth, J. Anton, *Rev. Mod. Phys.* **2003**; *75*, 35.
[21] J. R. Taylor, *An introduction to error analysis. The study of uncertainties in physical measurements*, University Science Books, Sausalito, **1997**.
[22] M. R. Gherase, E. D. Desouza, M. J. Farquharson, F. E. McNeill, C.-Y. Kim, D. E. B. Fleming, *Physiol. Meas.* **2013**; *34*, 1163.
[23] M. L. Garg, J. Singh, H. R. Verma, N. Singh, P. C. Mangal, P. N. Trehan, *J. Phys. B: At. Mol. Phys.* **1984**; *17*, 577.
[24] http://physics.nist.gov/PhysRefData/Xcom/html/xcom1.html
[25] B. Gawdzik, T. Matynia, E. Chmielewska, *J. Appl. Polym. Sci.* **2001**; *82*, 2003.
[26] V. Hicks, *J. Appl. Phys.* **1941**; *12*, 364.
[27] M. Sabel, H. Aichinger, *Phys. Med. Biol.* **1996**; *41*, 315.
[28] P. C. Johns, M. J. Yaffe, *Phys. Med. Biol.* **1987**; *32*, 675.